Nano Research 2016, 9(7): 1983–1993
DOI 10.1007/s12274-016-1089-7
Research Article
ISSN 1998-0124
CN 11-5974/O4

Nitrogen-doped graphene nanosheets as reactive water purification membranes

Yanbiao Liu[1] (✉), Ling Yu[1], Choon Nam Ong[1], and Jianping Xie[2] (✉)

[1] *NUS Environmental Research Institute, National University of Singapore, 117411, Singapore*
[2] *Department of Chemical and Biomolecular Engineering, National University of Singapore, 117585, Singapore*

Received: 4 March 2016
Revised: 28 March 2016
Accepted: 1 April 2016

KEYWORDS
persulfate activation,
nitrogen-doped graphene,
phenol oxidation,
convective flow,
batch system

ABSTRACT

Oxidation of organic pollutants by sulfate radicals produced via activation of persulfate has emerged as a promising advanced oxidation technology to address various challenging environmental issues. The development of an effective, environmentally-friendly, metal-free catalyst is the key to this technology. Additionally, a supported catalyst design is more advantageous than conventional suspended powder catalysts from the point of view of mass transfer and practical engineering applications (e.g. post-use separation). In this study, a metal-free N-doped reduced graphene oxide (N-rGO) catalyst was prepared via a facile hydrothermal method. N-rGO filters were then synthesized by facile vacuum filtration, such that water can flow through nanochannels within the filters. Various advanced characterization techniques were employed to obtain structural and compositional information of the as-synthesized N-rGO filters. An optimized phenol oxidative flux of 0.036 ± 0.002 mmol·h^{-1} was obtained by metal-free catalytic activation of persulfate at an influent persulfate concentration of 1.0 mmol·L^{-1} and filter weight of 15 mg, while a N-free rGO filter demonstrated negligible phenol oxidation capability under similar conditions. Compared to a conventional batch system, the flow-through design demonstrates obviously enhanced oxidation kinetics (0.036 vs. 0.010 mmol·h^{-1}), mainly due to the liquid flow through the filter leading to convection-enhanced transfer of the target molecule to the filter active sites. Overall, the results exemplified the advantages of organic compound removal by catalytic activation of persulfate using a metal-free catalyst in flow-through mode, and demonstrated the potential of N-rGO filters for practical environmental applications.

1 Introduction

Rapid modern industrial development has had a significant impact on the environment and led to several serious current environmental problems. In particular, phenol or phenolic compounds are widely

Address correspondence to Yanbiao Liu, eriliuyb@nus.edu.sg; Jianping Xie, chexiej@nus.edu.sg

produced and consumed in various fields such as the refinery, petrochemical, and pharmaceutical industries [1]. Contamination of water bodies by these phenolic compounds has therefore been identified as a problem of growing concern in recent decades [2]. To address this challenging issue, various technologies [3–10], including physical adsorption, electro-oxidation, Fenton-like reactions, and photocatalytic and membrane processes, have been extensively developed and screened. However, some conventional treatment technologies, such as adsorption, may not be effective towards the removal and/or degradation of these phenolic compounds. Even some state-of-the-art membrane technologies (e.g. reverse and forward osmosis) demonstrate only limited removal of phenol (<50%) due to the small size of the phenol molecule and its neutral state in aqueous solution [11]. Therefore, the development of cost-effective and efficiently controlled routes for phenolic compound removal is highly desirable.

Advanced oxidation processes (AOPs) are considered one of the most promising approaches for the removal and mineralization of various refractory organic pollutants [4, 6, 12]. Among them, catalytic oxidation by sulfate radicals ($SO_4^{\bullet-}$) produced by persulfate or peroxymonosulfate activation has emerged as a promising technique [13]. Compared to hydroxyl radicals (OH•) produced in photocatalytic and Fenton-like processes, $SO_4^{\bullet-}$ has a comparable or even higher oxidative potential (2.5–3.1 V for $SO_4^{\bullet-}$ vs. 2.7 V for OH•) and can adapt to a wider pH range [14]. Although the persulfate anion ($S_2O_8^{2-}$) alone is a strong oxidizer (with an oxidation potential of 2.01 V [15], higher than that of 1.76 V for H_2O_2 [16]), its reaction kinetics are sluggish towards the oxidation of some recalcitrant contaminants. Alternatively, $SO_4^{\bullet-}$ generation can significantly improve the efficiency and efficacy of persulfate oxidation. Some catalysts [17–22], such as transition metals (e.g. ferrous iron), chelated metals (e.g. Fe(III)–EDTA), and metal oxides (e.g. iron, cobalt, and manganese oxide), are capable of initiating $SO_4^{\bullet-}$ generation. However, considering the relatively high energy consumption (from providing heat and UV light) and potential environmental risks (e.g. leaching of toxic heavy metal ions), the development of alternative, equally/more effective, environmentally-friendly, metal-free catalysts to avoid these adverse effects has attracted recent interest in the water treatment community.

Graphene is a 2D one-atom-thick layer of graphite with an sp^2-hybridized carbon configuration [23]. The fascinating physical and chemical properties of graphene, such as large specific surface area (up to 2,630 $m^2 \cdot g^{-1}$), superior thermal conductivity (up to 5,300 $W \cdot m^{-1} \cdot K^{-1}$), strong mechanical stability (ultimate tensile strength of 130 GPa), rapid carrier mobility (theoretically potential limits of up to 200,000 $cm^2 \cdot V^{-1} \cdot s^{-1}$), and solution processability, have been well documented [24–30]. For instance, graphene (or reduced graphene oxide, rGO) has been proven to be an excellent sorbent for aromatic pollutant removal (e.g. via π–π interactions and/or hydrophobic effects). Wang et al. reported that both the reduction degree and chemical structure of target compounds affect the adsorption performance of graphene [31]. Besides serving as an ideal scaffold for hosting catalysts (e.g. TiO_2 [32] and ZnO [33]), graphene (or rGO) itself can also be directly used as a catalyst to activate persulfate and produce $SO_4^{\bullet-}$ for organic degradation [14], although the efficiency is limited. It has been reported that doping heteroatoms (e.g. N) into the graphene honeycomb network can result in novel catalytic properties, create more active sites, and hence greatly increase the catalytic activity compared to that of pristine graphene [34–41]. For example, N doping will influence the charge distribution and spin density of graphene carbon atoms, producing additional "activated regions" on the graphene surface [42]. A well-designed study performed by Guo et al. eventually revealed the active sites of N-doped carbon materials for the oxygen reduction reaction (ORR) to be carbon atoms with Lewis basicity comparable to that of pyridinic N [43]. Other studies further proved that N-doped graphene or rGO powder showed significantly improved performance for persulfate activation. For example, experimental and theoretical studies by Duan et al. showed that doped graphene can efficiently activate peroxymonosulfate to produce $SO_4^{\bullet-}$ and demonstrates obviously enhanced activity compared with other state-of-the-art metal-based catalysts (e.g. Co_3O_4) [44–46]. Wang et al. reported that the degradation rate constant of bisphenol A over a suspended N-doped rGO (N-rGO) catalyst was

0.71 min^{-1} in the presence of 0.6 $mmol \cdot L^{-1}$ persulfate, which was approximately 700 times higher than that of N-free rGO (0.001 min^{-1}) [47].

Most previously reported N-doped graphene or rGO catalysts are in the powder form and have been used in a conventional batch reactor for persulfate activation. However, separation of these ultrafine nanoscale powder catalysts after reaction is costly and tedious, hindering the practical engineering applications of such promising metal-free catalysts. Furthermore, mass transfer of target molecules towards the active sites of the catalyst is predominantly controlled by a relatively slow diffusion process [48], which significantly limits the oxidative kinetics. Recent advancements in GO and rGO-based membrane technologies [49–53] have inspired us to utilize stacked doped graphene or rGO nanosheets as membranes for water filtration in the liquid phase in the presence of persulfate. In such a filtration system, the reaction mechanism involves three primary steps: 1) mass transfer to the N-rGO filter surface; 2) adsorption onto and desorption from the filter; and 3) $SO_4^{\bullet-}$ generation and pollutant degradation. The first step is usually the rate-determining step. Liu and Vecitis previously proved that a filtration system is advantageous compared to a conventional batch system due to the liquid flow through the filter, which leads to convection-enhanced transfer of the target molecule towards the filter surface [54]. In this study, N-rGO filters were first synthesized by vacuum filtration and characterized by various advanced characterization techniques. Next, the performance of the filters was evaluated by the degradation of selected phenolic compound (e.g. phenol), and the effects of persulfate concentration and filter thickness were examined in this proof-of-concept study. Finally, the degradation kinetics of the N-rGO filters were studied and compared with those of a conventional batch system.

2 Experimental

2.1 Chemicals and materials

Sodium persulfate (≥98%, $Na_2S_2O_8$), phenol (≥98%, C_6H_6O), and tetracycline (≥98%, $C_{22}H_{24}N_2O_8 \cdot xH_2O$) were purchased from Sigma-Aldrich (Singapore). Ammonia solution (25%) was purchased from Merck (Singapore). Ethanol (95%–97%) and N-methyl-2-pyrrolidone (NMP, ≥99.0%) were purchased from VWR (Singapore). Suwannee River humic acid (SR-HA) was purchased from the International Humic Substances Society (St. Paul, MN). Aqueous solutions were prepared with deionized water (DI-H_2O) from a TKA water purification system with a resistivity of ≥ 18.2 $M\Omega \cdot cm^{-1}$. Graphene oxide (GO, oxygen content ~40%, layer size ~60 μm × 60 μm, as provided by the manufacturer) powder was purchased from Suzhou Graphene Nanotech. Co. Ltd. (China).

2.2 Filter synthesis

The synthesis of N-rGO powder followed a recently published protocol with some modifications [55]. Commercial GO was used as a precursor. A certain amount of GO powder was dispersed at a concentration of 2.0 $mg \cdot mL^{-1}$ in DI-H_2O using a digital Branson probe sonicator for 10 min, followed by the addition of 2.0 mL ammonia under vigorous stirring. Then, the mixture solution was transferred into a Teflon-lined autoclave and kept in a Memmert UF30 drying oven for 15 h at 180 °C. Column-like hydrogel products (Fig. S1 in the Electronic Supplementary Material (ESM)) were obtained as a result of the high surface energy of the rGO nanosheets, which causes them to aggregate under the high temperature and pressure conditions. These hydrogels were collected by vacuum filtration onto a 0.45 μm Hach mixed-cellulose ester filter paper (D = 47 mm) and washed with a copious amount of DI-H_2O to remove any adsorbed residues (e.g. $NH_3 \cdot H_2O$). For comparison, N-free rGO was prepared by a similar route, without the addition of $NH_3 \cdot H_2O$.

rGO and N-rGO filters were then prepared by dispersing certain amounts of the rGO and N-rGO powders in NMP at a concentration of 0.5 $mg \cdot mL^{-1}$, followed by probe sonication for 60 min to ensure that the catalysts were well-dispersed. Then, the mixed solutions were loaded onto 5 μm Millipore JMWP PTFE filters by vacuum filtration and sequentially washed with 100 mL ethanol and 250 mL DI-H_2O.

2.3 Filter characterization

The morphology and crystal phase of the filter materials were examined using a JEOL JSM-6700F

field emission scanning electric microscope and Bruker D8 Advance Powder X-ray diffractometer, respectively. X-ray photoelectron spectroscopy (XPS) was performed on a Kratos AXIS Ultra^{DLD} (Kratos, UK) with monochromatic Al Kα radiation (75 W, 15 kV, $h\nu$ = 1,486.71 eV) under 1 × 10^{-9} Torr vacuum conditions, and all XPS binding energies were calibrated relative to C1s (C–C bond) at 285.0 eV.

2.4 Filtration system

The synthesized rGO or N-rGO filter was placed into a commercial 47 mm Whatman membrane filter holder (Fig. S2 in the ESM). After sealing the filtration casing and priming with water, a Masterflex peristaltic pump was used to drive DI-H_2O through the filter to rinse it and calibrate the flow rate. The fluid to be treated (e.g. 0.5 mmol·L^{-1} phenol) was then flowed through the filter at an influent flow rate of 1.5 mL·min^{-1} to achieve adsorption saturation (i.e. the effluent and influent concentration were equal), with the aim of eliminating the contribution of adsorption on compound removal. Thereafter, the same concentration of fluid with certain amount of $Na_2S_2O_8$ was passed through the filter to induce the catalytic oxidation process for the removal of target compounds. Effluent aliquots were collected and analyzed on an Waldbronn Agilent 1290 UHPLC system (Germany) coupled to a 6540 quadrupole-time of flight (Q-TOF) mass detector equipped with a dual jet stream electrospray ionization source, for details refer to a recent study [56].

3 Results and discussion

3.1 Characterization of rGO and N-rGO

Figures 1(a) and 1(b) compare the field emission scanning electron microscopy (FESEM) images of the rGO and N-rGO filters. The data suggest that both samples demonstrate crumpled sheet-like microstructures, typical of graphene. It seems that the GO powders (before loading to the filter, Fig. S3 in the ESM) are more crumpled compared to the other reduced counterparts due to the presence of a large amount of oxy-functional groups (e.g. hydroxyl and carboxylic groups). It was expected that most of these oxy-functional groups in GO could be reduced via

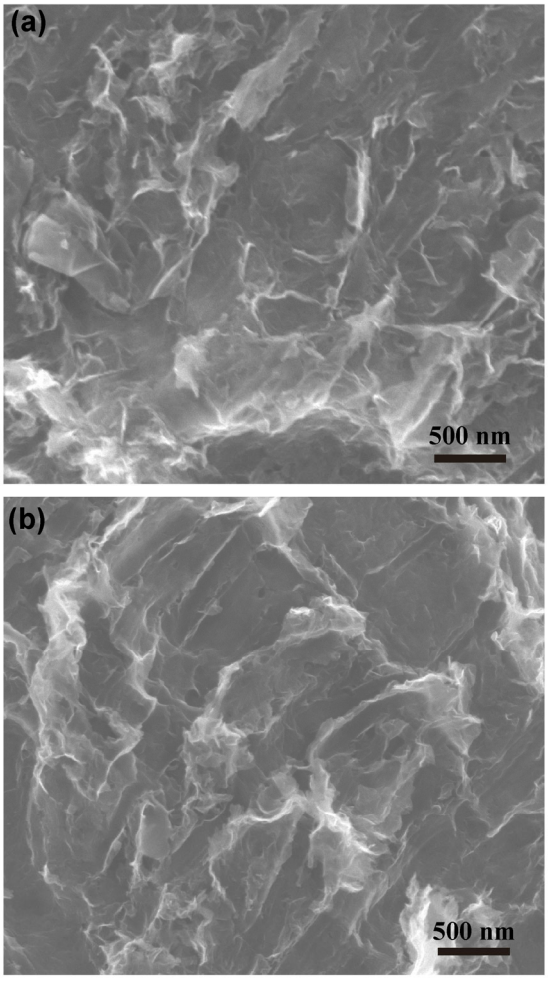

Figure 1 FESEM images of (a) rGO filter and (b) N-rGO filter.

hydrothermal treatment in a "water-only" system [57], since overheated supercritical water can act as a reducing agent, as reported previously by Zhou et al. As anticipated, the flexible and scalable rGO and N-rGO filters (Fig. S4 in the ESM) displayed relatively flat surface morphologies, possibly due to the removal of some functional groups by supercritical water, NH_3·H_2O, or both. No obvious difference can be observed between the rGO and N-rGO samples, suggesting that N doping did not significantly change the rGO surface morphology. Conversion from GO to rGO or N-rGO can be further verified by the X-ray diffraction (XRD) results, as shown in Fig. S5 in the ESM. The strong characteristic peak centered at 2θ = 9.3° corresponds to the typical (002) diffraction peak of GO. The interlayer distance of 0.49 nm was slightly larger than that of pristine graphite (0.35 nm), which is due to the presence of oxy-functional groups. However,

the characteristic peak at 2θ = 9.3° has completely disappeared in the spectra of the rGO and N-rGO samples, indicating that the graphitic crystal structure was restored after reduction. No other characteristic peaks from rGO or doped rGO can be seen due to strong interference from the polytetrafluoroethylene (PTFE) support and/or limited thickness of the as-synthesized filters (~25 μm).

XPS measurements were also acquired to obtain chemical compositional information of the rGO and N-rGO filters. As shown in Fig. 2, the XPS survey pattern of the N-rGO sample clearly demonstrates the presence of C1s, O1s, and N1s, whereas only C1s and O1s are observed for the rGO sample. These data unambiguously verify the successful doping of N into rGO. The atomic ratio of N in N-rGO was determined to be 3.59% from the XPS data (Table S1 in the ESM), which was within the typical N doping range of 1%–15% [42, 58]. As can be seen from the high-resolution N1s scan (Fig. 2(b)), the sample has a relatively higher content of pyrrolic N centered at 399.8 eV (56.0%), a lower content of pyridinic N at 398.4 eV (25.4%), and a much lower amount of quaternary N at 401.1 eV (13.4%). The ratio of pyrrolic N:pyridinic N:quaternary N was estimated to be 1:0.45:0.24 based on peak area integration. This value was different to the deconvolution results reported by Wang et al. [55], who claimed that pyridinic N was the major component. Figure 2(c) shows the high-resolution C1s scan, which indicates the existence of C–C (285.0 eV, 61.4%), C–N (285.8 eV, 14.3%), C–O (286.7 eV, 17.8%), C=O (288.0 eV, 3.8%), and O–C=O (289.2 eV, 2.9%) bonds in N-rGO. The high-resolution O1s scan can be further deconvoluted into C=O (530.7 eV, 17.2%), C–O–C (531.8 eV, 28.6%), C–OH (533.1 eV, 51.2%), and H_2O (535.4 eV, 3.0%). Additionally, elemental mapping of the N-rGO filter by energy dispersive spectroscopy (EDS) confirmed the presence and uniform distribution of N within the rGO matrices, further indicating successful N doping (Fig. S6 in the ESM).

3.2 Catalytic oxidation of phenol

The persulfate activation capability of the N-rGO filter was investigated using phenol as the model

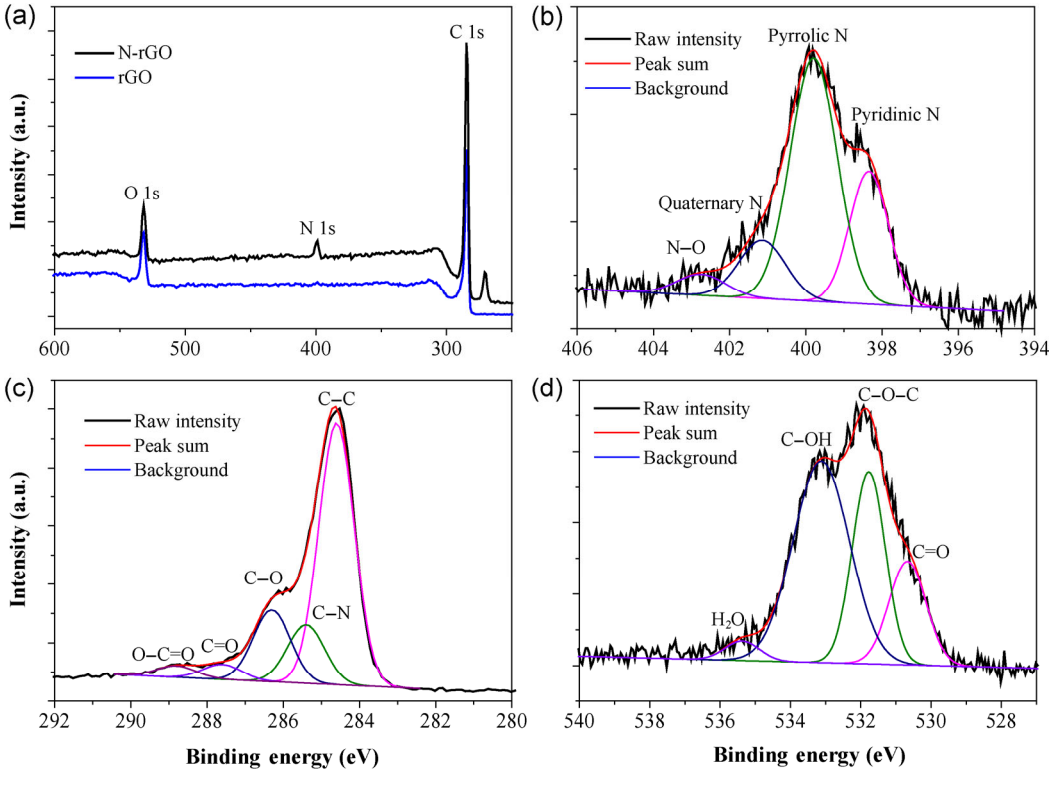

Figure 2 (a) Comparison of the XPS survey patterns of rGO and N-rGO filters, and high-resolution XPS scans of (b) N1s, (c) C1s, and (d) O1s for the as-synthesized N-rGO filter.

aromatic compound. To verify whether phenol could be removed by persulfate alone without applying the N-rGO filtration system, a control experiment was conducted by directly mixing 1 mmol·L^{-1} $Na_2S_2O_8$ with 0.5 mmol·L^{-1} phenol in a batch reactor. The results show that there were negligible changes in phenol concentration over 3 h, indicating that persulfate alone cannot generate sulfate radicals ($SO_4^{\bullet-}$) or oxidize phenol. Another control experiment was carried out in the absence of persulfate, where breakthrough (i.e. adsorption saturation) of a 15 mg N-rGO filter occurred over 2 h continuous filtration at a flow rate of 1.5 mL·min^{-1}, suggesting that physical adsorption to the N-rGO filter was not sustainable for phenol treatment (Fig. 3(a), left panel). Furthermore, the presence of both persulfate and the rGO filter (after adsorption saturation) resulted in only negligible phenol removal (<4%), indicating that rGO cannot effectively activate persulfate because only a limited number of activate sites are available on the filter. However, the effluent phenol concentration was obviously decreased by the N-rGO filters after the addition of various concentrations of persulfate. Only minimal oxidation was observed at an initial persulfate concentration of 0.1 mmol·L^{-1}, and at >0.1 mmol·L^{-1} the phenol oxidation flux increased with increasing persulfate concentration to a maximum of 0.036 ± 0.002 mmol·h^{-1} at 1.0 mmol·L^{-1}. The stable oxidation flux over the following 3 h of continuous operation (after adsorption saturation) and the absence of complete breakthrough suggested that the primary removal mechanism for phenol was catalytic oxidation by $SO_4^{\bullet-}$ rather than physical adsorption. Increasing the persulfate concentration above 1.0 mmol·L^{-1} reduced the filter performance due to side reactions, e.g. redundant persulfate may react with generated $SO_4^{\bullet-}$ to produce the sulfate ions (SO_4^{2-}). Moreover, the obtained oxidation flux of 0.036 mmol·h^{-1} is comparable to that of a recently reported electrochemical carbon nanotube filter system [56], for which a phenol oxidation flux of 0.043 mmol·h^{-1} was obtained under optimized operational conditions. However, the electrochemical filter system required an additional applied electricity input (2.5 V total cell potential), pre-pumping of O_2 (dissolved oxygen concentration of 44 mg·L^{-1}) into the influent solution, and then pumping of the

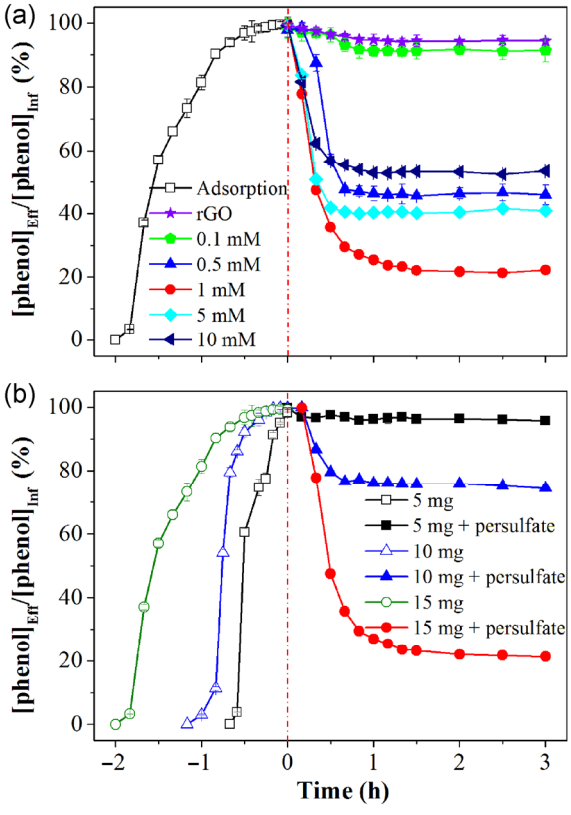

Figure 3 Kinetic data for the adsorption and degradation of phenol by the rGO and N-rGO filters: effect of (a) persulfate concentration and (b) filter thickness. Experimental conditions: flow rate 1.5 mL·min^{-1} and pH 6.5.

fluid through the filter (flow rate of 1.5 mL·min^{-1}), leading to increased energy consumption (~0.2 kW·h·m^{-3}). The major advantage of the proposed N-rGO filter technology is that the energy consumption was significantly minimized and comparable phenol oxidation is still obtained. In the current system, only pumping energy was necessary. At a flow rate of 1.5 mL·min^{-1}, pumping efficiency of 75%, and common backpressure of 15 kPa, the energy required for pumping was calculated to be 1.5 J, only ~2% that of the energy needed for the previously reported electrochemical filter system.

As well as the persulfate concentration, filter thickness is an important parameter affecting the N-rGO filter performance. Since the filter was prepared via a facile vacuum filtration route, its thickness was proportional to the weight of initial N-rGO (or rGO) (Fig. S7 in the ESM). As shown in Fig. 3(b), by keeping the initial persulfate concentration constant (1.0 mmol·L^{-1}), the phenol oxidation flux was found to increase with

initial N-rGO weight from 5 (0.0015 mmol·h^{-1}) to 15 mg (0.036 mmol·h^{-1}), since the phenol oxidation performance is directly related to the amount of $SO_4^{\bullet-}$ and a thicker filter will produce more radicals. However, further increasing the weight to 25 mg resulted in deterioration in filter performance (0.011 mmol·h^{-1}, Fig. S8 in the ESM), which can be explained by side reactions, e.g. consumption of $SO_4^{\bullet-}$ by persulfate. These data highlight the importance of filter thickness; there is a trade-off between water flux and filter performance, e.g. a thicker filter is usually accompanied by a lower water flux.

To further evaluate the performance of the N-rGO filter in the presence of natural organic matter (NOM), SR-HA was selected as a model compound for dissolved NOM due to the prevalence of humic-like substances throughout surface water and wastewater effluent. The results demonstrate that the addition of SR-HA negatively affects phenol oxidation (see Fig. S9 in the ESM). The phenol oxidation flux at 5 mg·L^{-1} SR-HA (a typical NOM concentration in water bodies) was decreased by 18% when compared with that obtained in the absence of SR-HA. This decrease in phenol oxidation flux can be attributed to competitive adsorption on the N-rGO filter and the $SO_4^{\bullet-}$ scavenging effect of NOM. The decrease in phenol oxidative flux was higher than the NOM:phenol ratio (i.e. 10%), suggesting that the larger NOM fraction likely adsorbs strongly to the N-rGO filter and may block a certain amount of surface active sites [47].

The XPS spectrum of the N-rGO filter after 3 h continuous operation was also recorded, as shown in Fig. 4. The atomic ratio of N was significantly decreased from 3.6% (before filtration) to 0.9% (after filtration), with pyrrolic, pyridinic, and quaternary N decreased by 78%, 72%, and 67%, respectively, when comparing the corresponding peak areas before and after phenol filtration (see Figs. 4(a) and 4(b)). This is mainly due to N loss during the reaction via a N oxidation process [40], which could alter the content of different N configurations. Another explanation for the decreased N content may be due to the build-up of some organic (possibly phenol oxidation by-products) and/or inorganic (possibly sodium persulfate salt due

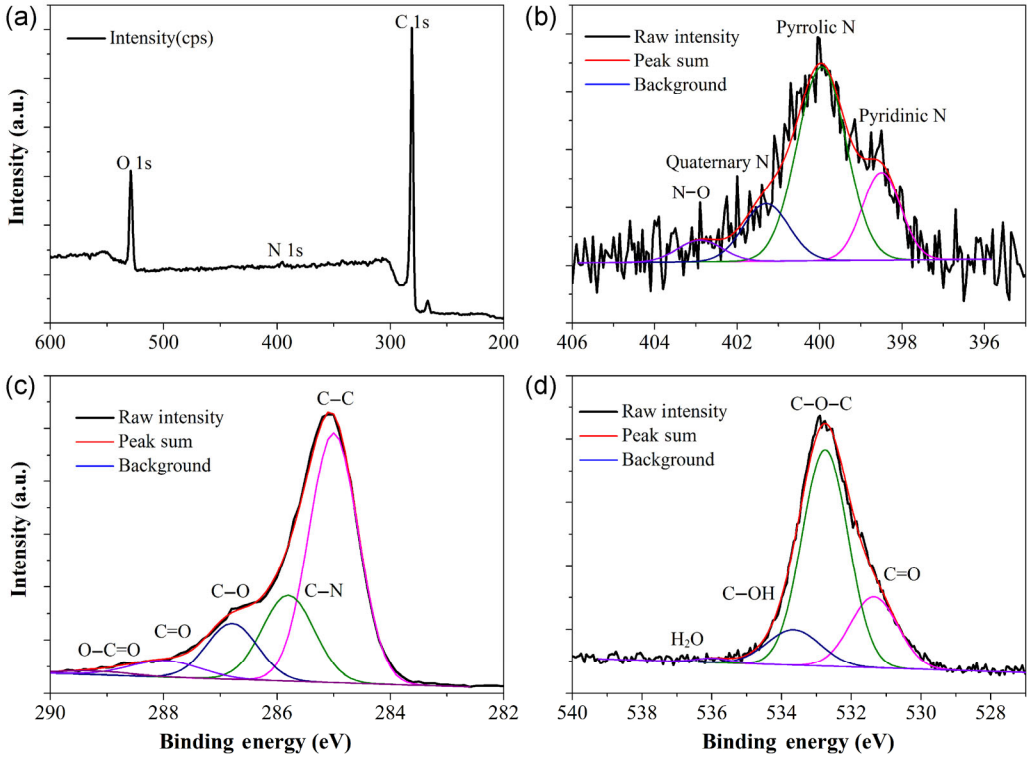

Figure 4 (a) Survey, (b) N1s, (c) C1s, and (d) O1s of the N-rGO filter after 3 h continuous phenol filtration at a flow rate of 1.5 mL·min^{-1} and 1 mmol·L^{-1} persulfate.

to its low water solubility) substances on the N-rGO surface, which may have blocked the N below (Fig. S10 in the ESM). The ratio of pyrrolic N:pyridinic N:quaternary N was calculated to be 1:0.35:0.27 based on peak areas, indicating that the ratio of pyridinic N decreased while that of quaternary N increased compared with the N-rGO sample before phenol treatment (Fig. 4(b)). Comparison of the high-resolution C1s patterns reveals an increase in the C–C (58.6%) and C–N (21.2%) carbon peaks, and a decrease in the C–O (13.5%), C=O (5.4%), and O–C=O (1.1%) carbon peaks (Fig. 4(c)). The most significant change in the high-resolution O1s scan is the sharp decrease in intensity of the C–OH peak centered at 533.1 eV (from 51.2% before phenol filtration to 12.3% after phenol filtration) and significant increase in intensity of the C–O–C peak centered at 531.8 eV (from 28.6% before phenol filtration to 64.9% after phenol filtration), as shown in Fig. 4(d). These data suggest that, compared to other oxygen-containing functional groups, the relative content of –OH groups detached from aromatic carbon decreases after phenol oxidation, possibly due to a dehydration reaction with the hydroxyl group of phenol molecules. The evident enhancement in the C–O–C peak may be due to the accumulation of phenol oxidation by-products on the N-rGO surface.

The effective and efficient removal of phenol revealed the potential of N-rGO filter technology for water purification. To further explore its potential for water treatment, the N-rGO filter was subjected to the antibiotic tetracycline, a typical pharmaceutical and personal care product (PPCP) commonly detected in water bodies. Under the optimized experimental conditions (i.e. 1 mmol·L^{-1} persulfate and 15 mg N-rGO), the oxidative flux of 0.5 mmol·L^{-1} tetracycline was determined to be 0.020 ± 0.0011 mmol·h^{-1} (Fig. S11 in the ESM), just 57% that of the phenol oxidation flux. This was because tetracycline has a relatively complex molecular structure when compared with phenol; also, complete oxidization of a tetracycline molecule requires 106 electrons while only 28 electrons are required to completely oxidize a phenol molecule, and hence, only partial oxidation of tetracycline can be expected [47]. The tetracycline filtration results also demonstrated that ~50% influent tetracycline molecules can be oxidized via a single-pass through the N-rGO filter with a hydraulic retention time τ of <1 s, indicating that the filter may be promising for the treatment of other refractory contaminants with aromatic structures and low detection concentrations.

3.3 Comparison of the convective flow system with a conventional batch system

The filtration system setup is important in the removal of organic compounds. To evaluate whether phenol can be equally oxidized by N-rGO in a conventional batch system, the same amount of N-rGO (15 mg) was dispersed in a 150 mL solution 0.5 mmol·L^{-1} phenol and 1 mmol·L^{-1} $Na_2S_2O_8$. As shown in Fig. 5, N-rGO powder clearly exhibited enhanced oxidation performance compared with that of rGO. For instance, 43.8% phenol can be oxidized by N-rGO within 3 h, while

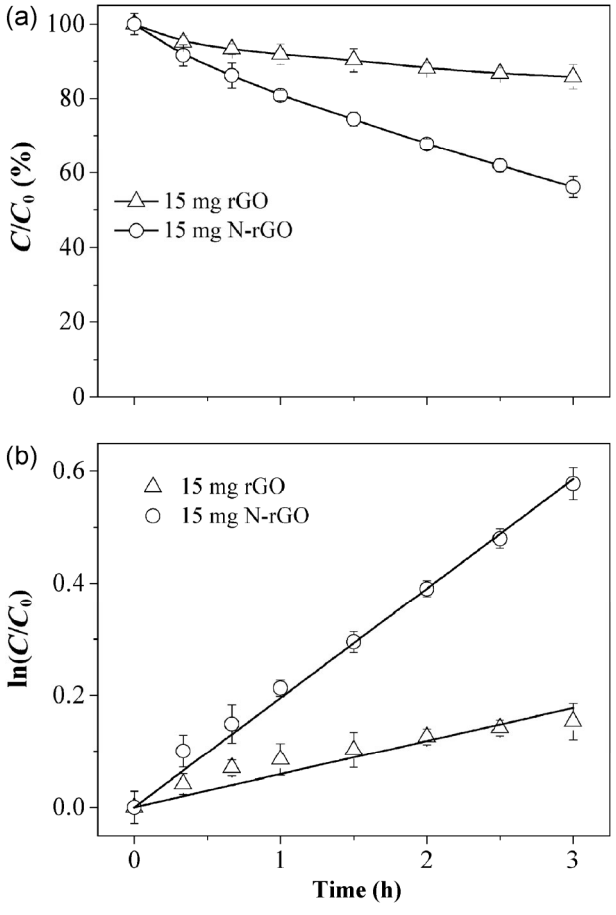

Figure 5 Comparison of (a) phenol removal and (b) corresponding kinetic curves using N-rGO and rGO powder in a conventional batch reactor. Experimental conditions: 15 mg catalyst, 150 mL 0.5 mmol·L^{-1} phenol solution, 1 mmol·L^{-1} persulfate, and 150 rpm shaking speed.

only 14.2% phenol can be removed over the same period by rGO via physical adsorption. However, the limited sorbents of rGO (e.g. 15 mg) results in a relatively low absolute adsorption capacity, and in turn rGO adsorption saturation will inevitably happen within a short time (e.g. 2 h). To quantitatively describe the reaction process, the Langmuir–Hinshelwood (L–H) model was employed. The results demonstrate that both materials tested in this study satisfactorily follow the L–H model, with corresponding kinetics constants (k), normalized by the solution volume and concentration, identified as 0.010 and 0.0035 mmol·h^{-1} for N-rGO and rGO, respectively. It is noteworthy that k for the convective flow system was 3.6 times higher than that of the batch system for the same amount of N-rGO sample (0.036 mmol·h^{-1} for filtration vs. 0.010 mmol·h^{-1} for batch), which could be ascribed to enhanced mass transfer in the filtration compared to the batch system, resulting in more rapid transport of phenol molecules to the N-rGO filter surface. However, there was only a negligible change (<10%) in the oxidation kinetics of the rGO filters, regardless of the reaction system (filtration or batch), since the dominant pollutant removal mechanism for the rGO filter was physical adsorption rather than oxidation.

4 Conclusions

In summary, an N-rGO filter was developed and applied to the removal of selected organic compounds by physical adsorption and catalytic oxidation. Compared with its nanoparticle counterparts, the N-rGO filter demonstrates evidently enhanced mass transfer rate and oxidation kinetics, and avoids drawbacks, such as separation and recovery, associated with conventional powder catalysts. Overall, the experimental results presented herein quantitatively exemplify the advantages of using N-rGO materials in flow-through filtration systems for water purification.

Acknowledgements

This work is supported by GE-NUS research grant (WBS number of R-706-005-004-592). We thank Professor Heqing Tang at South Central University for Nationalities and Dr. Neil Moe at GE Water and Process Technologies for their valuable technical discussions and professional suggestions.

Electronic Supplementary Material: Supplementary material (1 table and 11 figures) is available in the online version of this article at http://dx.doi.org/10.1007/s12274-016-1089-7.

References

[1] Michałowicz, J.; Duda, W. Phenols—Sources and toxicity. *Pol. J. Environ. Stud.* **2007**, *16*, 347–362.

[2] Hladik, M. L.; Focazio, M. J.; Engle, M. Discharges of produced waters from oil and gas extraction via wastewater treatment plants are sources of disinfection by-products to receiving streams. *Sci. Total Environ.* **2014**, *466–467*, 1085–1093.

[3] Mukherjee, R.; De, S. Adsorptive removal of phenolic compounds using cellulose acetate phthalate-alumina nanoparticle mixed matrix membrane. *J. Hazard. Mater.* **2014**, *265*, 8–19.

[4] Zhang, A.; Li, Y. M. Removal of phenolic endocrine disrupting compounds from waste activated sludge using UV, H_2O_2, and UV/H_2O_2 oxidation processes: Effects of reaction conditions and sludge matrix. *Sci. Total Environ.* **2014**, *493*, 307–323.

[5] Al Hashemi, W.; Maraqa, M. A.; Rao, M. V.; Hossain, M. M. Characterization and removal of phenolic compounds from condensate-oil refinery wastewater. *Desalin. Water Treat.* **2015**, *54*, 660–671.

[6] Iboukhoulef, H.; Amrane, A.; Kadi, H. Removal of phenolic compounds from olive mill wastewater by a Fenton-like system H_2O_2/Cu(II)—Thermodynamic and kinetic modeling. *Desalin. Water Treat.* **2016**, *57*, 1874–1879.

[7] Adhoum, N.; Monser, L. Decolourization and removal of phenolic compounds from olive mill wastewater by electrocoagulation. *Chem. Eng. Process.* **2004**, *43*, 1281–1287.

[8] Achak, M.; Hafidi, A.; Ouazzani, N.; Sayadi, S.; Mandi, L. Low cost biosorbent "banana peel" for the removal of phenolic compounds from olive mill wastewater: Kinetic and equilibrium studies. *J. Hazard. Mater.* **2009**, *166*, 117–125.

[9] Ersöz, A.; Denizli, A.; Şener, I.; Atilir, A.; Diltemiz, S.; Say, R. Removal of phenolic compounds with nitrophenol-imprinted polymer based on π–π and hydrogen-bonding interactions. *Sep. Purif. Technol.* **2004**, *38*, 173–179.

[10] Caza, N.; Bewtra, J. K.; Biswas, N.; Taylor, K. E. Removal of phenolic compounds from synthetic wastewater using soybean peroxidase. *Water Res.* **1999**, *33*, 3012–3018.

[11] Subramani, A.; Jacangelo, J. G. Emerging desalination technologies for water treatment: A critical review. *Water Res.* **2015**, *75*, 164–187.

[12] Saitoh, T.; Fukushima, K.; Miwa, A. Combined use of surfactant-induced coagulation of poly(allylamine hydrochloride) with peroxidase-mediated degradation for the rapid removal of estrogens and phenolic compounds from water. *Sep. Purif. Technol.* **2014**, *128*, 11–17.

[13] Indrawirawan, S.; Sun, H. Q.; Duan, X. G.; Wang, S. B. Nanocarbons in different structural dimensions (0–3D) for phenol adsorption and metal-free catalytic oxidation. *Appl. Catal. B: Environ.* **2015**, *179*, 352–362.

[14] Sun, H. Q.; Liu, S. Z.; Zhou, G. L.; Ang, H. M.; Tadé, M. O.; Wang, S. B. Reduced graphene oxide for catalytic oxidation of aqueous organic pollutants. *ACS Appl. Mater. Interfaces* **2012**, *4*, 5466–5471.

[15] Tsitonaki, A.; Petri, B.; Crimi, M.; Mosbæk, H.; Siegrist, R. L.; Bjerg, P. L. *In situ* chemical oxidation of contaminated soil and groundwater using persulfate: A review. *Crit. Rev. Environ. Sci. Technol.* **2010**, *40*, 55–91.

[16] Brillas, E.; Sirés, I.; Oturan, M. A. Electro-fenton process and related electrochemical technologies based on fenton's reaction chemistry. *Chem. Rev.* **2009**, *109*, 6570–6631.

[17] Yan, J. C.; Zhu, L. H.; Luo, Z. H.; Huang, Y. F.; Tang, H. Q.; Chen, M. F. Oxidative decomposition of organic pollutants by using persulfate with ferrous hydroxide colloids as efficient heterogeneous activator. *Sep. Purif. Technol.* **2013**, *106*, 8–14.

[18] Yan, J. C.; Lei, M.; Zhu, L. H.; Anjum, M. N.; Zou, J.; Tang, H. Q. Degradation of sulfamonomethoxine with Fe_3O_4 magnetic nanoparticles as heterogeneous activator of persulfate. *J. Hazard. Mater.* **2011**, *186*, 1398–1404.

[19] Fang, G. D.; Gao, J.; Dionysiou, D. D.; Liu, C.; Zhou, D. M. Activation of persulfate by quinones: Free radical reactions and implication for the degradation of PCBs. *Environ. Sci. Technol.* **2013**, *47*, 4605–4611.

[20] Fang, G. D.; Liu, C.; Gao, J.; Dionysiou, D. D.; Zhou, D. M. Manipulation of persistent free radicals in biochar to activate persulfate for contaminant degradation. *Environ. Sci. Technol.* **2015**, *49*, 5645–5653.

[21] Zhong, H.; Brusseau, M. L.; Wang, Y. K.; Yan, N.; Quig, L.; Johnson, G. R. *In-situ* activation of persulfate by iron filings and degradation of 1,4-dioxane. *Water Res.* **2015**, *83*, 104–111.

[22] Gao, Y. W.; Zhang, Z. Y.; Li, S. M.; Liu, J.; Yao, L. Y.; Li, Y. X.; Zhang, H. Insights into the mechanism of heterogeneous activation of persulfate with a clay/iron-based catalyst under visible LED light irradiation. *Appl. Catal. B: Environ.* **2016**, *185*, 22–30.

[23] Novoselov, K. S.; Geim, A. K.; Morozov, S. V.; Jiang, D.; Zhang, Y.; Dubonos, S. V.; Grigorieva, I. V.; Firsov, A. A. Electric field effect in atomically thin carbon films. *Science* **2004**, *306*, 666–669.

[24] Chen, S. S.; Wu, Q. Z.; Mishra, C.; Kang, J. Y.; Zhang, H. J.; Cho, K.; Cai, W. W.; Balandin, A. A.; Ruoff, R. S. Thermal conductivity of isotopically modified graphene. *Nat. Mater.* **2012**, *11*, 203–207.

[25] Bi, H. C.; Xie, X.; Yin, K. B.; Zhou, Y. L.; Wan, S.; He, L. B.; Xu, F.; Banhart, F.; Sun, L. T.; Ruoff, R. S. Spongy graphene as a highly efficient and recyclable sorbent for oils and organic solvents. *Adv. Funct. Mater.* **2012**, *22*, 4421–4425.

[26] Bi, H. C.; Yin, K. B.; Xie, X.; Zhou, Y. L.; Wan, N.; Xu, F.; Banhart, F.; Sun, L. T.; Ruoff, R. S. Low temperature casting of graphene with high compressive strength. *Adv. Mater.* **2012**, *24*, 5124–5129.

[27] Ren, W. C.; Cheng, H. M. The global growth of graphene. *Nat. Nanotechnol.* **2014**, *9*, 726–730.

[28] Geim, A. K.; Novoselov, K. S. The rise of graphene. *Nat. Mater.* **2007**, *6*, 183–191.

[29] Lonkar, S. P.; Deshmukh, Y. S.; Abdala, A. A. Recent advances in chemical modifications of graphene. *Nano Res.* **2015**, *8*, 1039–1074.

[30] Peng, W. C.; Li, X. Y. Synthesis of a sulfur-graphene composite as an enhanced metal-free photocatalyst. *Nano Res.* **2013**, *6*, 286–292.

[31] Wang, X. B.; Huang, S. S.; Zhu, L. H.; Tian, X. L.; Li, S. H.; Tang, H. Q. Correlation between the adsorption ability and reduction degree of graphene oxide and tuning of adsorption of phenolic compounds. *Carbon* **2014**, *69*, 101–112.

[32] Chen, C.; Cai, W. M.; Long, M. C.; Zhou, B. X.; Wu, Y. H.; Wu, D. Y.; Feng, Y. J. Synthesis of visible-light responsive graphene oxide/TiO_2 composites with p/n heterojunction. *ACS Nano* **2010**, *4*, 6425–6432.

[33] Gao, P.; Liu, Z. Y.; Sun, D. D. The synergetic effect of sulfonated graphene and silver as co-catalysts for highly efficient photocatalytic hydrogen production of ZnO nanorods. *J. Mater. Chem. A* **2013**, *1*, 14262–14269.

[34] Chen, S.; Duan, J. J.; Tang, Y. H.; Jin, B.; Qiao, S. Z. Molybdenum sulfide clusters-nitrogen-doped graphene hybrid hydrogel film as an efficient three-dimensional hydrogen evolution electrocatalyst. *Nano Energy* **2015**, *11*, 11–18.

[35] Zhou, R. F.; Qiao, S. Z. Silver/nitrogen-doped graphene interaction and its effect on electrocatalytic oxygen reduction. *Chem. Mater.* **2014**, *26*, 5868–5873.

[36] Yin, H.; Zhang, C. Z.; Liu, F.; Hou, Y. L. Hybrid of iron nitride and nitrogen-doped graphene aerogel as synergistic catalyst for oxygen reduction reaction. *Adv. Funct. Mater.* **2014**, *24*, 2930–2937.

[37] Tian, G. L.; Zhao, M. Q.; Yu, D. S.; Kong, X. Y.; Huang, J. Q.; Zhang, Q.; Wei, F. Nitrogen-doped graphene/carbon nanotube hybrids: *In situ* formation on bifunctional catalysts and their superior electrocatalytic activity for oxygen evolution/reduction reaction. *Small* **2014**, *10*, 2251–2259.

[38] Tang, C.; Zhang, Q.; Zhao, M. Q.; Huang, J. Q.; Cheng, X. B.; Tian, G. L.; Peng, H. J.; Wei, F. Nitrogen-doped aligned carbon nanotube/graphene sandwiches: Facile catalytic growth on bifunctional natural catalysts and their applications as scaffolds for high-rate lithium-sulfur batteries. *Adv. Mater.* **2014**, *26*, 6100–6105.

[39] Duan, J. J.; Chen, S.; Dai, S.; Qiao, S. Z. Shape control of Mn_3O_4 nanoparticles on nitrogen-doped graphene for enhanced oxygen reduction activity. *Adv. Funct. Mater.* **2014**, *24*, 2072–2078.

[40] Xing, T.; Zheng, Y.; Li, L. H.; Cowie, B. C. C.; Gunzelmann, D.; Qiao, S. Z.; Huang, S. M.; Chen, Y. Observation of active sites for oxygen reduction reaction on nitrogen-doped multilayer graphene. *ACS Nano* **2014**, *8*, 6856–6862.

[41] Jiao, Y.; Zheng, Y.; Jaroniec, M.; Qiao, S. Z. Origin of the electrocatalytic oxygen reduction activity of graphene-based catalysts: A roadmap to achieve the best performance. *J. Am. Chem. Soc.* **2014**, *136*, 4394–4403.

[42] Wang, H. B.; Maiyalagan, T.; Wang, X. Review on recent progress in nitrogen-doped graphene: Synthesis, characterization, and its potential applications. *ACS Catal.* **2012**, *2*, 781–794.

[43] Guo, D. H.; Shibuya, R.; Akiba, C.; Saji, S.; Kondo, T.; Nakamura, J. Active sites of nitrogen-doped carbon materials for oxygen reduction reaction clarified using model catalysts. *Science* **2016**, *351*, 361–365.

[44] Duan, X. G.; O'Donnell, K.; Sun, H. Q.; Wang, Y. X.; Wang, S. B. Sulfur and nitrogen co-doped graphene for metal-free catalytic oxidation reactions. *Small* **2015**, *11*, 3036–3044.

[45] Duan, X. G.; Ao, Z. M.; Sun, H. Q.; Indrawirawan, S.; Wang, Y. X.; Kang, J.; Liang, F. L.; Zhu, Z. H.; Wang, S. B. Nitrogen-doped graphene for generation and evolution of reactive radicals by metal-free catalysis. *ACS Appl. Mater. Interfaces* **2015**, *7*, 4169–4178.

[46] Duan, X. G.; Indrawirawan, S.; Sun, H. Q.; Wang, S. B. Effects of nitrogen-, boron-, and phosphorus-doping or codoping on metal-free graphene catalysis. *Catal. Today* **2015**, *249*, 184–191.

[47] Liu, Y. B.; Liu, H.; Zhou, Z.; Wang, T. R.; Ong, C. N.; Vecitis, C. D. Degradation of the common aqueous antibiotic tetracycline using a carbon nanotube electrochemical filter. *Environ. Sci. Technol.* **2015**, *49*, 7974–7980.

[48] Bard, A. J.; Faulkner, L. R. *Electrochemical Methods: Fundamentals and Applications*, 2nd ed.; Wiley: New York, 2001.

[49] Hu, M.; Mi, B. X. Enabling graphene oxide nanosheets as water separation membranes. *Environ. Sci. Technol.* **2013**, *47*, 3715–3723.

[50] Liu, H.; Liu, J.; Liu, Y. B.; Bertoldi, K.; Vecitis, C. D. Quantitative 2D electrooxidative carbon nanotube filter model: Insight into reactive sites. *Carbon* **2014**, *80*, 651–664.

[51] Sun, P. Z.; Zheng, F.; Zhu, M.; Song, Z. G.; Wang, K. L.; Zhong, M. L.; Wu, D. H.; Little, R. B.; Xu, Z. P.; Zhu, H. W. Selective trans-membrane transport of alkali and alkaline earth cations through graphene oxide membranes based on cation–π interactions. *ACS Nano* **2014**, *8*, 850–859.

[52] Joshi, R. K.; Carbone, P.; Wang, F. C.; Kravets, V. G.; Su, Y.; Grigorieva, I. V.; Wu, H. A.; Geim, A. K.; Nair, R. R. Precise and ultrafast molecular sieving through graphene oxide membranes. *Science* **2014**, *343*, 752–754.

[53] Mi, B. X. Graphene oxide membranes for ionic and molecular sieving. *Science* **2014**, *343*, 740–742.

[54] Liu, H.; Vecitis, C. D. Reactive transport mechanism for organic oxidation during electrochemical filtration: Mass-transfer, physical adsorption, and electron-transfer. *J. Phys. Chem. C* **2012**, *116*, 374–383.

[55] Wang, X. B.; Qin, Y. L.; Zhu, L. H.; Tang, H. Q. Nitrogen-doped reduced graphene oxide as a bifunctional material for removing bisphenols: Synergistic effect between adsorption and catalysis. *Environ. Sci. Technol.* **2015**, *49*, 6855–6864.

[56] Liu, Y. B.; Xie, J. P.; Ong, C. N.; Vecitis, C. D.; Zhou, Z. Electrochemical wastewater treatment with carbon nanotube filters coupled with *in situ* generated H_2O_2. *Environ. Sci.: Water Res. Technol.* **2015**, *1*, 769–778.

[57] Zhou, Y.; Bao, Q. L.; Tang, L. A. L.; Zhong, Y. L.; Loh, K. P. Hydrothermal dehydration for the "green" reduction of exfoliated graphene oxide to graphene and demonstration of tunable optical limiting properties. *Chem. Mater.* **2009**, *21*, 2950–2956.

[58] Sahu, V.; Grover, S.; Tulachan, B.; Sharma, M.; Srivastava, G.; Roy, M.; Saxena, M.; Sethy, N.; Bhargava, K.; Philip, D. et al. Heavily nitrogen doped, graphene supercapacitor from silk cocoon. *Electrochim. Acta* **2015**, *160*, 244–253.